

Active Temporal Control of Radiative Heat Transfer with Graphene Nanodisks

Lauren Zundel¹ and Alejandro Manjavacas¹^{*}

Department of Physics and Astronomy, University of New Mexico, Albuquerque, New Mexico 87106, USA



(Received 23 January 2020; revised manuscript received 20 March 2020; accepted 21 April 2020; published 21 May 2020)

The ability to dynamically control the radiative transfer of heat at the nanoscale holds the key to the development of a diverse number of technologies, ranging from nanoscale thermal-management systems to improved thermophotovoltaic devices. Recently, graphene has emerged as an ideal material to achieve this goal, since it can be electrically doped to support surface plasmons, collective oscillations of the conduction electrons. These resonances produce large and spectrally narrow optical cross sections, which dictate the emission and absorption properties of the graphene nanostructure and, thus, the heat that it radiatively exchanges with other objects and the environment. For attainable levels of doping, the plasmons supported by graphene nanostructures naturally lie in the midinfrared part of the spectrum, which is the most relevant wavelength range for radiative heat transfer under realistic temperatures. Furthermore, these resonances are actively tunable, thus providing full dynamic control over the heat transfer. Motivated by this great potential, we present a comprehensive analysis of the temporal evolution of the radiative heat transfer between arrangements of graphene nanodisks, showing that it is possible to exploit the tunability of these structures to obtain actively controlled heat transfer scenarios not possible with conventional passive nanostructures. The results of this work provide a framework for achieving fully dynamical control over nanoscale radiative heat transfer and thus provide fundamental insights into this process.

DOI: 10.1103/PhysRevApplied.13.054054

I. INTRODUCTION

In the absence of conduction and convection, the mechanism by which objects reach thermal equilibrium with one another and their surroundings is radiative heat transfer [1]. At the macroscale, the radiative heat transfer between objects is accurately described by Planck's law [2]. However, when the distance that separates them is reduced to well below the so-called thermal wavelength, $\lambda_T = 2\pi\hbar c/(k_B T)$, the radiative heat transfer can exceed the values predicted by the black-body model as a result of the dominant role played, in this limit, by the near-field or evanescent modes [3–17]. Similarly, when the dimensions of the objects become smaller than λ_T , the presence of strong electromagnetic resonances can result in absorption cross sections that are, at resonant wavelengths, much larger than the physical area of the nanostructure [18], thus enabling a radiative heat transfer that again surpasses the black-body limit [19–33]. Graphene nanostructures constitute a paradigmatic example of this. These systems, when doped with carriers by means of, for example, electrostatic gating, can support collective oscillations of the conduction electrons, so-called surface plasmons [34,35], which result in extraordinarily large-absorption cross sections [36,37]. For attainable levels of doping, these excitations

naturally lie in the midinfrared part of the electromagnetic spectrum [38,39], which is the most relevant spectral range for radiative heat transfer under realistic temperatures. Due to these exceptional properties, graphene has become an ideal platform for radiative heat transfer [40–42]. As an additional benefit, the frequency of graphene plasmons can be actively tuned by changing the doping level [43,44], which sets these systems apart from conventional plasmonic nanostructures that must be refabricated with different geometrical or material properties to change their plasmonic response. Graphene plasmons can be modulated with time scales as fast as a few picoseconds, as recently demonstrated [45,46], thus enabling the possibility of switching the doping level during the radiative heat-transfer process. This active tunability has therefore motivated a tremendous effort focused on manipulating radiative heat transfer between graphene nanostructures [47–57], with the goal of both gaining greater fundamental understanding of this process and advancing applications benefiting from active control over radiative transfer, such as thermal camouflage [55]. Despite this research effort, the majority of the work has been focused on studying the thermal conductance between graphene nanostructures, rather than the dynamics of the radiative heat transfer involved [58]. However, an analysis of the time dependence of this transfer is necessary to fully exploit the tunability of graphene nanostructures for actively controlling the radiative heat transfer.

*manjavacas@unm.edu

Motivated by this need, here we study the temporal evolution of the temperature of graphene nanodisks under a variety of time-dependent doping profiles and different geometrical arrangements. Exploiting this fully dynamical approach, we predict actively controlled heat-transfer scenarios that are inaccessible for conventional nontunable plasmonic structures. The results of this work help to shed light on the use of graphene structures for the active control of radiative heat transfer, thus complementing other approaches explored in the past involving phase-change materials [59,60], structures with magneto-optical responses [61,62], and nonlinear frequency mixing [63].

II. RESULTS AND DISCUSSION

The system under consideration consists of an ensemble of N graphene nanodisks that exchange heat with one another and the surrounding environment through radiation. We consider all the nanodisks to be placed in the same plane, which, although imposing a minimum separation as compared with a stacking geometry, facilitates a potential experimental verification of our theoretical predictions. We can determine the temporal evolution of the temperature T_i of disk i by finding the power absorbed by the disk, which we denote by \mathcal{P}_i . In order to do so, we work within the dipolar approximation [64–67], which is justified due to the large mismatch between the size of the disks (on the order of tens of nanometers) and the relevant wavelengths (on the order of microns) and employ the fluctuational-electrodynamics framework in which each disk is modeled as a fluctuating point dipole [20,26,68]. Under these approximations, \mathcal{P}_i can be calculated as an integral over frequencies ω (for a detailed derivation, see Appendix A),

$$\begin{aligned} \mathcal{P}_i = & \frac{2\hbar}{\pi} \int_0^\infty d\omega \omega \text{Tr} \left[\sum_j \text{Im} \left(\mathbf{A}_{ij} \text{Im}\{\chi_j\} \mathbf{C}_{ij}^+ \right) N_j \right. \\ & \left. + \sum_{jj'} \text{Im} \left(\mathbf{B}_{ij} \text{Im}\{\mathbf{G}_{jj'} + \mathbf{G}_{jj'}^0\} \mathbf{D}_{ij'}^+ \right) N_0 \right], \quad (1) \end{aligned}$$

where the plus sign (“+”) represents the conjugate transpose and Tr indicates the trace over Cartesian components, while $N_i = n(\omega, T_i) + 1/2$, in which $n(\omega, T) = [\exp(\hbar\omega/k_B T) - 1]^{-1}$ is the Bose-Einstein distribution. T_i is the temperature of particle i and T_0 is the temperature of the environment, which, in this work, we take to be vacuum at 300 K. The different matrices appearing in this expression are defined as follows: $\mathbf{A} = [\mathcal{I} - \boldsymbol{\alpha}\mathbf{G}]^{-1}$, $\mathbf{B} = \mathbf{A}\boldsymbol{\alpha}$, $\mathbf{C} = (\mathbf{G} + \mathbf{G}^0)\mathbf{A}$, and $\mathbf{D} = \mathcal{I} + \mathbf{C}\boldsymbol{\alpha}$, where \mathcal{I} is the $3N \times 3N$ identity matrix, \mathbf{G} is the dipole-dipole interaction tensor, $\mathbf{G}^0 = (2i/3)k^3\mathcal{I}$ with $k = \omega/c$, and $\boldsymbol{\chi} = \boldsymbol{\alpha} - \mathbf{G}^0\boldsymbol{\alpha}^+\boldsymbol{\alpha}$. Furthermore, $\boldsymbol{\alpha}$ is a diagonal matrix containing the different Cartesian components of

the polarizability of each of the nanodisks. Due to the two-dimensional character of the nanodisks, we assume that the out-of-plane component of the polarizability can always be neglected. On the other hand, we model the in-plane components as $\alpha = [\alpha_0^{-1} - (2i/3)k^3]^{-1}$, where

$$\alpha_0 = \frac{8R^3\zeta^2}{(-1/\eta) - 2i\omega R/\sigma}, \quad (2)$$

is a quasistatic polarizability obtained using the plasmon wave-function formalism [69]. In this expression, R is the nanodisk radius, $\eta = -0.0728$, and $\zeta = 0.8508$ [37,69–72]. Furthermore, σ represents the electrical conductivity of graphene, which we take from the local limit of the random-phase approximation (RPA) for an extended graphene sheet [37]. The conductivity depends on the temperature of the disk and its electron mobility, which we set to $\mu = 3000 \text{ cm}^2/(\text{V s})$, a conservative value that is within experimental reach [73,74]. It also depends on the Fermi level E_F of the graphene nanodisk, which characterizes the doping level of the nanostructure. Although, here, for simplicity, we assume the nanodisks to be self-standing, the expression for α_0 given in Eq. (2) can be readily modified to account for the effect of a substrate, as shown in Refs. [37,69–71]. Specifically, for a substrate with dielectric function ε , η is replaced by $\eta(\varepsilon + 1)/2$. Therefore, the effect of the substrate on the response of the nanodisk is mainly a shift of its resonance frequency, which can always be compensated by appropriately changing its Fermi level.

Once \mathcal{P}_i is calculated using Eq. (1), the temporal evolution of the temperature of nanodisk i can be determined by solving the differential equation

$$\frac{\partial T_i}{\partial t} = \frac{\mathcal{P}_i(T_0, T_1, \dots, T_N)}{C_{p,i}(T_i)}. \quad (3)$$

Here, $C_{p,i}$ represents the heat capacity of nanodisk i , which we calculate from the data for the specific heat of graphene compiled in Ref. [75], as explained in Appendix B. It is important to note that this expression assumes that, at all times, the electrons and the atomic lattice of the nanodisks are thermalized. This is justified, since, as opposed to Ref. [41], the distances between nanodisks considered in this work make the time scale over which heat is exchanged between them much larger than the electron-lattice thermalization time.

Throughout this work, we fix the size of the nanodisks to $R = 15 \text{ nm}$, which is large enough to ensure that nonlocal effects play a small role, as shown in Ref. [41], and choose a center-to-center distance of $a = 4R$. In order to inform the choice of Fermi levels that will maximize and minimize the heat transfer between the graphene nanodisks, we begin with a detailed analysis of the system of two nanodisks depicted in Fig. 1(a). We assume that disk 1 has initial temperature 400 K and a Fermi level denoted

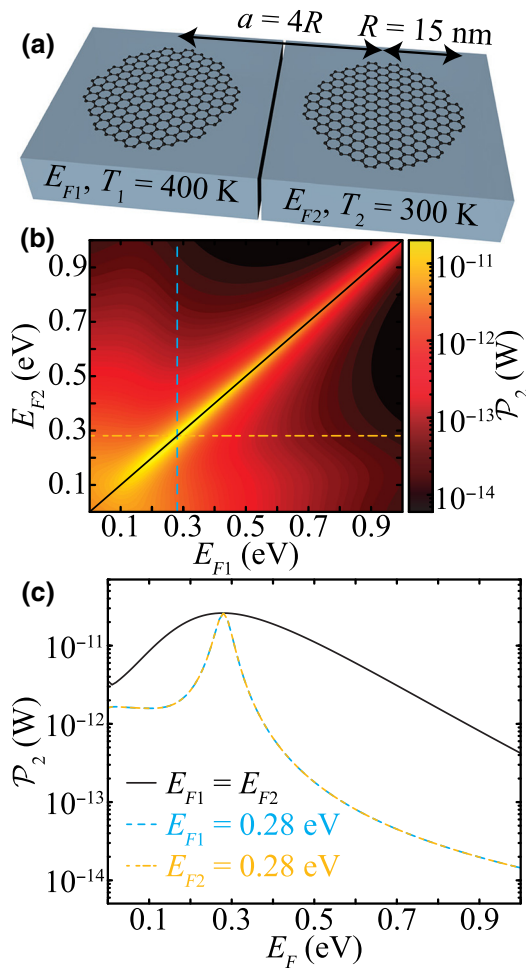


FIG. 1. Radiative heat transfer between two graphene nanodisks. (a) Schematics of the system under consideration, consisting of two graphene nanodisks of equal radius $R = 15$ nm, separated by a distance $a = 4R$. One disk has temperature $T_1 = 400$ K and Fermi level E_{F1} , while the other is at $T_2 = 300$ K with E_{F2} . The environment is held at $T_0 = 300$ K. (b) Power absorbed by disk 2 at a time $t = 0$ s as a function of E_{F1} and E_{F2} . (c) Line cuts from panel (b) for $E_{F1} = E_{F2}$ (black solid curve), $E_{F1} = 0.28$ eV (blue dashed curve), and $E_{F2} = 0.28$ eV (yellow dotted curve).

by E_{F1} , while disk 2 is initially at 300 K, and has Fermi level E_{F2} . Figure 1(b) shows the power absorbed by disk 2, \mathcal{P}_2 , at time $t = 0$ s, plotted as a function of the Fermi levels of both structures. Since disk 2 is initially thermalized with the environment, \mathcal{P}_2 coincides with the power transferred from disk 1 to disk 2. As expected, we find that \mathcal{P}_2 is maximized along the line $E_{F1} = E_{F2}$, for which the plasmon resonances of the two nanodisks perfectly overlap with one another. On the other hand, when the two Fermi levels have very high contrast, the power absorbed by disk 2 is dramatically decreased, effectively thermally isolating the disks from one another, due to the large mismatch between the plasmon resonances of the two nanodisks.

Furthermore, there is a particular Fermi level along the $E_{F1} = E_{F2}$ line that produces the maximum power transfer between the two disks. This optimum condition is clearly shown by the black solid curve in Fig. 1(c), which represents a line cut of the results of panel (b) along the line $E_{F1} = E_{F2}$. This maximum comes as a result of the interplay between the Bose-Einstein distribution, which, for a given temperature, decays with increasing energy, and the strength and spectral position of the plasmon resonances, both of which increase with the Fermi level. In particular, for the system considered here, the Fermi level producing the maximum power transfer is $E_F = 0.28$ eV. However, this value depends on the temperatures of the disks through the Bose-Einstein distribution in Eq. (1), as well as on the size of the nanodisks and their separation from one another, as discussed in Appendix C.

Since our goal is to achieve complete control over the radiative heat transfer between disks, we need to not only determine the optimal Fermi levels to maximize the radiative heat transfer between the two disks but also choose Fermi levels that can minimize this transfer. To that end, in Fig. 1(c), we also analyze two other cuts of the data plotted in panel (b). Specifically, the blue dashed curve shows a cut for $E_{F1} = 0.28$ eV, while the yellow dotted curve displays the results for $E_{F2} = 0.28$ eV. As expected, for a Fermi level of 0.28 eV (i.e., when the two disks have the same Fermi level), these curves meet the black solid one but, for all other doping levels, the power transfer becomes smaller. Such a decrease is more pronounced for larger Fermi levels, which produce a larger spectral separation of the plasmon resonances of the two nanodisks. Interestingly, the power transfer does not vanish as one of the Fermi levels goes to zero due to the interband transitions, which contribute to the polarizability of the nanodisks at energies larger than twice the value of their Fermi level. This highlights the importance of using an accurate model of the conductivity capable of capturing the effect of interband transitions [37], as explained in Appendix D. This analysis tells us that, in order to switch the radiative heat transfer between two disks off, the Fermi levels of the two disks should be chosen such that there is a large contrast between them. Here, the value that we choose to achieve such a situation is $E_F = 1.0$ eV, which results in a power transfer that is nearly 3 orders of magnitude less than the optimal case, but still remains within reasonable experimental reach for the electrostatic doping of graphene [37]. Importantly, any experimental verification of our predictions will require the use of a substrate that is simultaneously transparent in the relevant wavelength range and capable of providing enough thermal isolation to the system. In particular, the power exchanged conductively between the disks and the substrate has to be smaller than the radiative heat-transfer power shown in Fig. 1(c).

Once we have found the appropriate Fermi levels to switch the radiative heat transfer between two nanodisks

on and off, the next step is to study the temporal dynamics of this system of two disks under different doping scenarios. We perform this analysis in Fig. 2(a), for the

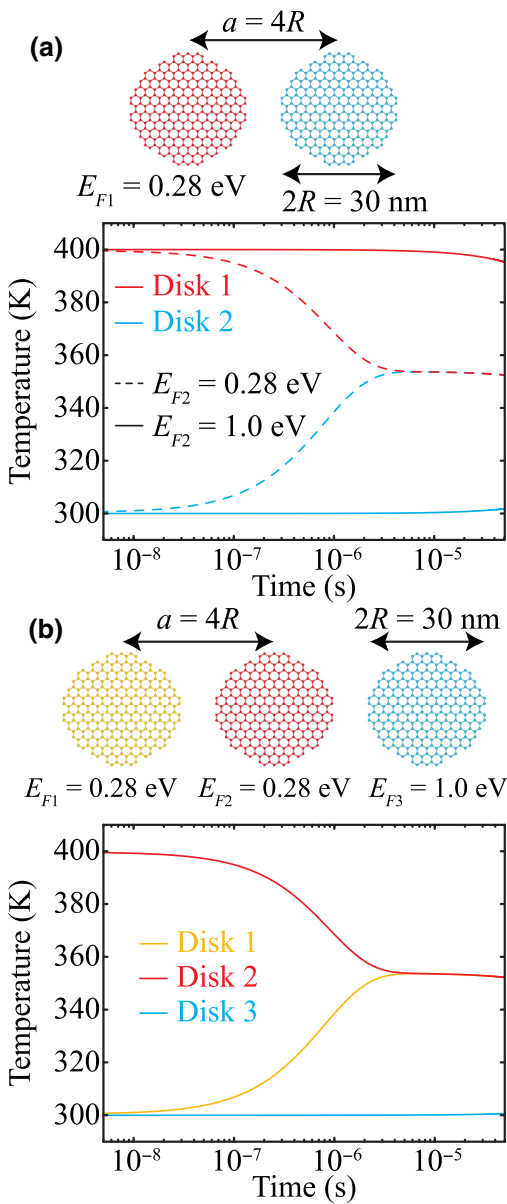


FIG. 2. Directed heat transfer. (a) Temporal evolution of the temperatures of two nanodisks of radius $R = 15 \text{ nm}$ and center-to-center separation $a = 4R$, as depicted in the upper schematics. One disk (red) begins at temperature $T_1 = 400 \text{ K}$ and has $E_{F1} = 0.28 \text{ eV}$, while the other disk (blue) begins at $T_2 = 300 \text{ K}$ with E_{F2} . The dashed curves correspond to the case in which $E_{F2} = 0.28 \text{ eV}$, while the solid ones show the temporal evolution when $E_{F2} = 1.0 \text{ eV}$. (b) Evolution of the temperatures for a chain of three nanodisks of the same size and separations as in (a), as shown by the schematics. The outer disks begin at a temperature $T_1 = T_3 = 300 \text{ K}$, whereas the center one starts at $T_2 = 400 \text{ K}$. One outer disk (yellow), and the center one (red) have Fermi levels $E_{F1} = E_{F2} = 0.28 \text{ eV}$, while the other outer disk (blue) has Fermi level $E_{F3} = 1.0 \text{ eV}$.

same geometry as in Fig. 1, as depicted by the upper schematics. We set the Fermi level of disk 1 to be $E_{F1} = 0.28 \text{ eV}$ and consider two different values for E_{F2} . When $E_{F2} = 0.28 \text{ eV}$, the value that maximizes the heat transfer between the two disks as per Fig. 1, the two disks thermalize in around 5 μs , as shown by the dashed curves (for the dynamics using other values of the Fermi level and electron mobility, see Appendices E and F). If, instead, the Fermi level of disk 2 is 1.0 eV, the temperatures of the two disks barely change from their initial values, even after ten times as much time, as shown by the solid curves. This illustrates the possibility of actively switching the radiative heat transfer between two disks on or off by controlling their Fermi levels.

The results of Fig. 2(a) open the door for more interesting scenarios, as recently proposed [48,56], in which, through a careful choice of the Fermi levels of each disk within an ensemble, it is possible to direct the radiative heat transfer in a desired direction. In order to analyze this possibility, in Fig. 2(b), we investigate the temporal dynamics of a system of three nanodisks with $R = 15 \text{ nm}$ and separation $a = 4R$, as shown by the upper schematics. We choose an initial temperature distribution in which the edge disks, denoted disk 1 (yellow) and disk 3 (blue), are thermalized with the environment (i.e., at 300 K), while the central disk, disk 2 (red), is at 400 K. Then, by setting the Fermi levels of disks 1 and 2 to 0.28 eV while keeping disk 3 at 1.0 eV, we can make the first two thermalize without impacting the temperature of the third one. Indeed, as shown by the red and yellow curves, disks 1 and 2 reach a thermal equilibrium between them in around 5 μs , as is the case for the two disks in panel (a). At the same time, disk 3 remains at a nearly constant temperature, even after 50 μs . This behavior proves the possibility of channeling heat toward a desired nanodisk, while minimally impacting the neighboring structures.

Building on this idea, we next consider the possibility of actively controlling the propagation of heat through a chain of nanodisks situated between a heat source and sink. Specifically, we analyze a chain of seven nanodisks with $R = 15 \text{ nm}$ and separation $a = 4R$, as shown in Fig. 3(a). Each of the nanodisks is set to a uniform Fermi level of $E_F = 0.28 \text{ eV}$ and begins at a temperature 300 K. On the left end of the chain, we place a disk acting as a heat source. This disk has the same geometrical properties as the ones in the chain but is held at a constant temperature of 400 K. Similarly, at the right end, we place an identical disk held at a constant temperature of 300 K, which acts as a heat sink. Then, by appropriately tuning the Fermi levels of the disks acting as heat source and sink, we can sequentially heat up and cool down the nanodisks of the chain. This scenario is analyzed in Figs. 3(b) and 3(c). Specifically, we initialize the system with a Fermi level of 0.28 eV for the source nanodisk and 1.0 eV for the sink one, as indicated by the red and blue curves of panel (b).

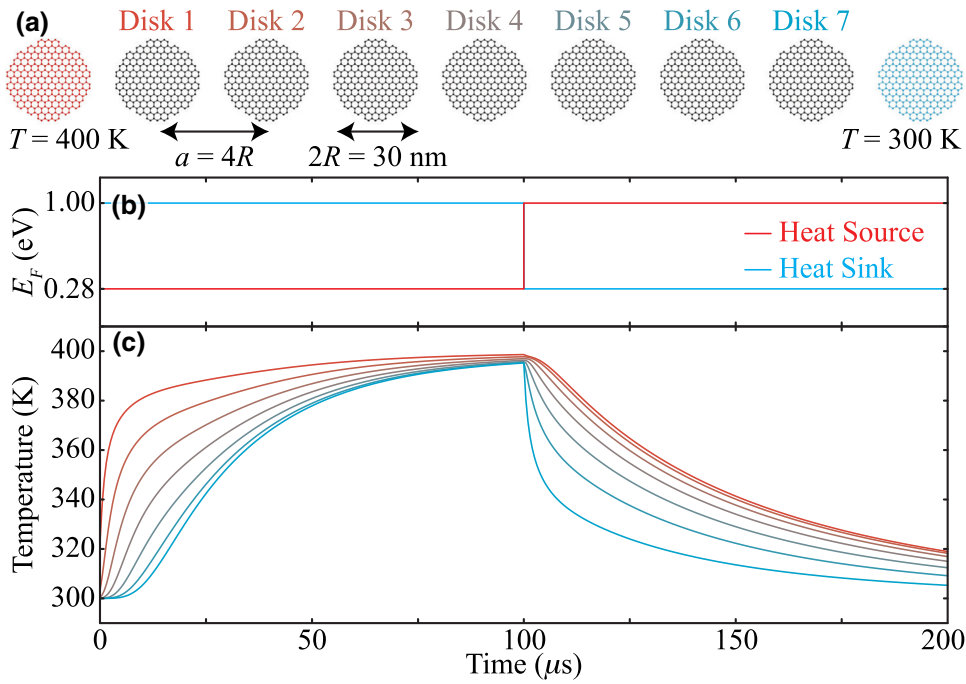


FIG. 3. Active control of heat propagation. (a) Schematics of the system under consideration, consisting of a chain of seven nanodisks of uniform radius $R = 15$ nm, center-to-center separation $a = 4R$, and doping level $E_F = 0.28$ eV. On the left end of the chain, there is a heat source (red) that is held at $T = 400$ K and, on the right one, a heat sink (blue) held at $T = 300$ K. The environment is at $T_0 = 300$ K. (b) Fermi levels of the heat source (red curve) and heat sink (blue curve) as a function of time. (c) Temporal evolution of the temperatures of disks 1–7. The colored curves match the corresponding labels of the disks that they represent from panel (a).

This configuration enables an efficient radiative heat transfer between the source nanodisk and the elements of the chain and, at the same time, isolates them from the sink. Therefore, as shown in panel (c), the temperature of each disk in the chain increases sequentially as a consequence of the heat cascading through the system. Once all of the disks in the chain have thermalized with the source, at a time $100 \mu\text{s}$ from the start of the heating phase, we swap the Fermi levels of the heat source and sink, so that the former is now at 1.0 eV and the latter at 0.28 eV. This change of the Fermi levels is assumed to be instantaneous on the time scale of the simulation since, as discussed before, it could be performed in a time that is orders of magnitude faster than the simulation time step [45,46]. The new doping configuration enables radiative heat transfer between the chain and the heat sink, while simultaneously isolating the system from the heat source. As in the heating phase, the temperature change propagates sequentially through the chain of nanodisks but, in this case, it flows from the one closest to the heat sink to the farthest. Interestingly, this thermalization process requires a slightly longer period of time than the heating phase. We attribute this asymmetry to the interplay between the frequency and the temperature dependence of the Bose-Einstein distribution function. The restoration of the disks to their initial temperature distribution makes it possible to repeat the heating and cooling phases an arbitrary number of times, thus showing the possibility of controlling the propagation of heat through the chain.

The last heat-transfer scenario we consider is the possibility of achieving a thermally isolated disk that is at

a very different temperature than its neighbors. In order to achieve this goal, we consider the geometry depicted in Fig. 4(a), consisting of a chain of five nanodisks of radius $R = 15$ nm and center-to-center separation $a = 4R$, surrounded on either side by a heat source held at a temperature of 400 K (red disks) and a heat sink kept at 300 K (blue disks), all of which are a distance $4R$ from the outermost disks of the chain. As shown in panels (b) and (c), initially, we set the Fermi level of all of the disks in the chain and the heat sources to 0.28 eV, while the two heat sinks are set to 1.0 eV. With this configuration, the disks in the chain can be efficiently heated by the sources while remaining isolated from the sinks. This is illustrated in Fig. 4(d), where we show the temporal evolution of the temperature of each of the disks. At a time $25 \mu\text{s}$, after the chain of disks has thermalized with the heat sources, we swap the Fermi levels of the sources and sinks, which allows us to couple the nanodisks of the chain to the heat sink and thus cool them down. However, at the same time, we also change the Fermi level of disk 3 to 1.0 eV, which thermally isolates it from the rest of the elements of the chain. Examining the temperature evolution after this change in the Fermi levels, we see that disks 1, 2, 4, and 5 cool down rapidly and thermalize with the heat sinks. On the other hand, disk 3 remains at its higher temperature, barely changing at all over a time interval of $50 \mu\text{s}$. These results show that, despite the large temperature gradient with its nearest neighbors, the central disk remains thermally isolated from them, thus opening the door to the achievement of exotic heat-transfer scenarios resulting in nontrivial temperature distributions.

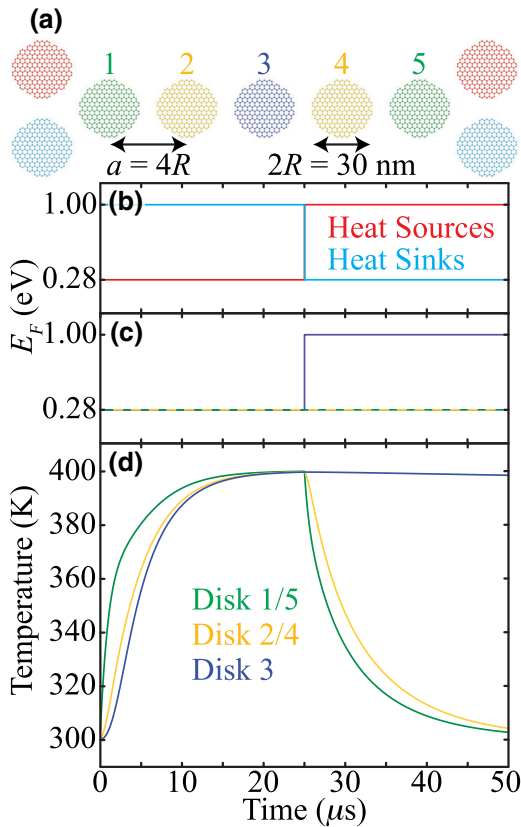


FIG. 4. Thermal isolation of a hot nanodisk. (a) Schematics of the system under consideration, consisting of a chain of five nanodisks of uniform radius $R = 15 \text{ nm}$ and center-to-center separation $a = 4R$. On both sides of the chain, there is a heat source (red) that is held at $T = 400 \text{ K}$ and a heat sink (blue) held at $T = 300 \text{ K}$, while the environment is held at $T_0 = 300 \text{ K}$. Both the heat source and sink are a distance of $4R$ from the closest disk in the chain. (b),(c) Temporal evolution of the Fermi levels of the heat sources and sinks (b) and the different disks in the chain (c). The colors of the different curves are matched with the colors of the disks in the schematics. (d) Temporal evolution of the temperature of each disk in the chain.

III. CONCLUSIONS

In summary, we have analyzed the temporal dynamics of the radiative heat transfer between different ensembles of graphene nanodisks. We have shown that, through the appropriate selection of the doping levels of two graphene nanodisks, it is possible to switch the radiative heat transfer between them on and off. This opens the door to the creation and control of exotic heat-transfer scenarios that it would not be possible to reach with conventional passive nanostructures. In particular, we have shown that it is possible to actively manipulate the propagation of heat through a chain of nanodisks as well as to heat up and thermally isolate a individual nanodisk from neighboring structures, thus creating strong temperature gradients.

Our study provides fundamental insights into the temporal dynamics of radiative heat transfer between graphene nanostructures, which can be exploited to actively manipulate this transfer process. Therefore, the results of this work can help in the development of a wide variety of technologies, including thermophotovoltaic devices, active thermal camouflage, and thermal-management techniques in nanoscale electronic circuitry, which may benefit from the active control of radiative heat transfer at the nanoscale [55,76,77].

ACKNOWLEDGMENTS

This work was sponsored by the U.S. National Science Foundation (Grants No. ECCS-1710697 and No. DMR-1941680). We acknowledge the UNM Center for Advanced Research Computing for computational resources used in this work. L.Z. acknowledges support from the Rayburn Reaching Up Fund, the New Mexico Space Grant Consortium, and the Department of Energy Computational Science Graduate Fellowship (Grant No. DE-SC0020347).

APPENDIX A: DERIVATION OF EQ. (1)

Working under the dipolar approximation, as described in the main text, the power absorbed by nanodisk i , \mathcal{P}_i , can be written in terms of the electric field at its position, \mathbf{E}_i , and its dipole moment, \mathbf{p}_i , as

$$\mathcal{P}_i = \left\langle \mathbf{E}_i(t) \cdot \frac{\partial \mathbf{p}_i(t)}{\partial t} \right\rangle,$$

where the angle brackets (“⟨⟩”) indicate an average over thermal fluctuations. Working in the frequency domain ω , defined via the Fourier transform $\mathbf{p}_i(t) = \int_{-\infty}^{\infty} (dw/2\pi) \mathbf{p}_i(\omega) e^{-i\omega t}$ for the dipole moment, and similarly for other quantities, we can rewrite \mathcal{P}_i as

$$\mathcal{P}_i = - \int_{-\infty}^{\infty} \frac{d\omega d\omega'}{(2\pi)^2} e^{-i(\omega-\omega')t} i\omega \langle \mathbf{E}_i^*(\omega') \cdot \mathbf{p}_i(\omega) \rangle, \quad (\text{A1})$$

where the asterisk (“*”) represents the complex conjugate. Following the approach described in Refs. [66,67] (see also Refs. [64,65]), both \mathbf{p}_i and \mathbf{E}_i can be written in terms of the sources that generate them, which are fluctuating dipoles \mathbf{p}^{fl} and fields \mathbf{E}^{fl} , as

$$\mathbf{p}_i = \sum_j \left[\mathbf{A}_{ij} \mathbf{p}_j^{\text{fl}} + \mathbf{B}_{ij} \mathbf{E}_j^{\text{fl}} \right]$$

and

$$\mathbf{E}_i = \sum_j \left[\mathbf{C}_{ij} \mathbf{p}_j^{\text{fl}} + \mathbf{D}_{ij} \mathbf{E}_j^{\text{fl}} \right].$$

The different matrices appearing in these equations are defined as $\mathbf{A} = [\mathcal{I} - \alpha\mathbf{G}]^{-1}$, $\mathbf{B} = \mathbf{A}\alpha$, $\mathbf{C} = (\mathbf{G} + \mathbf{G}^0)\mathbf{A}$, and $\mathbf{D} = \mathcal{I} + \mathbf{C}\alpha$, where \mathcal{I} is the $3N \times 3N$ identity matrix and α is a matrix that contains the polarizabilities of the nanodisks. As discussed in the main text, we neglect the out-of-plane component of the polarizability, while the in-plane components are modeled as $\alpha = [\alpha_0^{-1} - (2i/3)k^3]^{-1}$. In this expression, α_0 , which is given in Eq. (2), is a quasistatic polarizability obtained from the plasmon wave-function formalism [37,69–72].

Furthermore, $\mathbf{G}^0 = (2i/3)k^3\mathcal{I}$ and therefore $\mathbf{G}_{ij}^0 = (2i/3)k^3\delta_{ij}\mathcal{I}_{3 \times 3}$, where $k = \omega/c$ and $\mathcal{I}_{3 \times 3}$ is the 3×3 identity matrix. Moreover, \mathbf{G} is the dipole-dipole interaction tensor, the components of which are defined as

$$\begin{aligned}\mathbf{G}_{ij} &= \frac{e^{ikr_{ij}}}{r_{ij}^3} [(kr_{ij})^2 + ikr_{ij} - 1]\mathcal{I}_{3 \times 3} \\ &\quad - \frac{e^{ikr_{ij}}}{r_{ij}^3} [(kr_{ij})^2 + 3ikr_{ij} - 3]\frac{\mathbf{r}_{ij}\mathbf{r}_{ij}^+}{r_{ij}^2},\end{aligned}$$

when $i \neq j$ and 0 otherwise, where $\mathbf{r}_{ij} = \mathbf{r}_i - \mathbf{r}_j$ is the vector separating dipoles i and j , $r_{ij} = |\mathbf{r}_{ij}|$ and the plus sign (“ $+$ ”) represents the conjugate transpose.

Using these expressions in Eq. (A1), we can write the power absorbed by dipole i as

$$\begin{aligned}\mathcal{P}_i &= - \int_{-\infty}^{\infty} \frac{d\omega d\omega'}{(2\pi)^2} e^{-i(\omega-\omega')t} i\omega \\ &\quad \sum_{j,k} \left[\left[\mathbf{C}_{ij} \mathbf{p}_j^f + \mathbf{D}_{ij} \mathbf{E}_j^f \right]^+ \left[\mathbf{A}_{ik} \mathbf{p}_k^f + \mathbf{B}_{ik} \mathbf{E}_k^f \right] \right].\end{aligned}$$

At this point, we can invoke the fluctuation-dissipation theorem [78,79] (FDT) to perform the average over fluctuations. In particular, for the fluctuating dipole moments, the FDT takes the form

$$\langle \mathbf{p}_i(\omega) \mathbf{p}_j^+(\omega') \rangle = 4\pi\hbar\delta(\omega - \omega') \text{Im}\{\chi_i\} \delta_{ij} \left[n(\omega, T_i) + \frac{1}{2} \right],$$

where $n(\omega, T_i)$ is the Bose-Einstein distribution for temperature T_i and $\chi = \alpha - \mathbf{G}^0\alpha^+\alpha$. This expression takes into account the radiative corrections, although, given the large mismatch between the size of the graphene nanodisks and the relevant wavelengths, they do not play a relevant role for the systems under consideration. Similarly, for the electric field, we have

$$\begin{aligned}\langle \mathbf{E}_i(\omega) \mathbf{E}_j^+(\omega') \rangle &= 4\pi\hbar\delta(\omega - \omega') \text{Im}\{\mathbf{G}_{ij} + \mathbf{G}_{ij}^0\} \left[n(\omega, T_0) + \frac{1}{2} \right],\end{aligned}$$

where T_0 is the temperature of the environment. Applying the FDT to our expression and noting that there are no

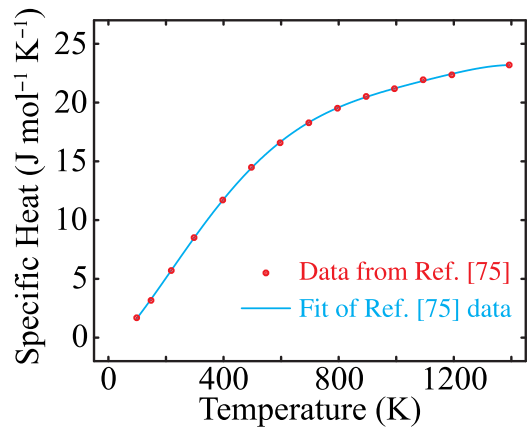


FIG. 5. Specific heat of graphene. The red dots correspond to measured data from Ref. [75], while the blue solid curve represents a polynomial fit to the data.

cross terms involving dipole and field fluctuations, since these are uncorrelated, we arrive at Eq. (1).

APPENDIX B: SPECIFIC HEAT OF GRAPHENE

As stated in Eq. (3), the calculation of the temporal evolution of the temperatures of the nanodisks requires knowledge of their heat capacities. To that end, here we use a polynomial fit to the data of the specific heat of graphene compiled in Ref. [75]. These data are plotted in Fig. 5 using red dots, together with the fit (blue curve).

APPENDIX C: OPTIMUM FERMI LEVEL

In Fig. 1(b) of the main text, we determine that, for a system of two nanodisks of radius $R = 15$ nm and center-to-center separation $a = 4R$, in which disk 1 begins at $T_1 = 400$ K and disk 2 begins at $T_2 = 300$ K, the Fermi level that produces the largest radiative heat transfer is $E_{F1} = E_{F2} = 0.28$ eV. In general, the optimum Fermi level depends on the size and separation between two nanodisks. To analyze this, we plot, in Fig. 6, the power absorbed by disk 2 as a function of the Fermi levels of both disks, for the same geometry described before, but with varying disk radii and separations. Specifically, the top, middle, and bottom rows correspond, respectively, to $R = 10$ nm, $R = 15$ nm, and $R = 20$ nm, while the left, center, and right columns represent $a = 3R$, $a = 4R$, and $a = 5R$, such that the panel in the middle corresponds to $R = 15$ nm, $a = 4R$, which is the geometry we consider in Fig. 1. As in the main text, the environment is vacuum at 300 K. As expected, in each of the panels, for a given Fermi level of either disk, the maximum power absorbed by disk 2 is achieved when the other disk has a matching value. Furthermore, as the size of or separation between the disks is increased, the optimum Fermi level is shifted to larger values.

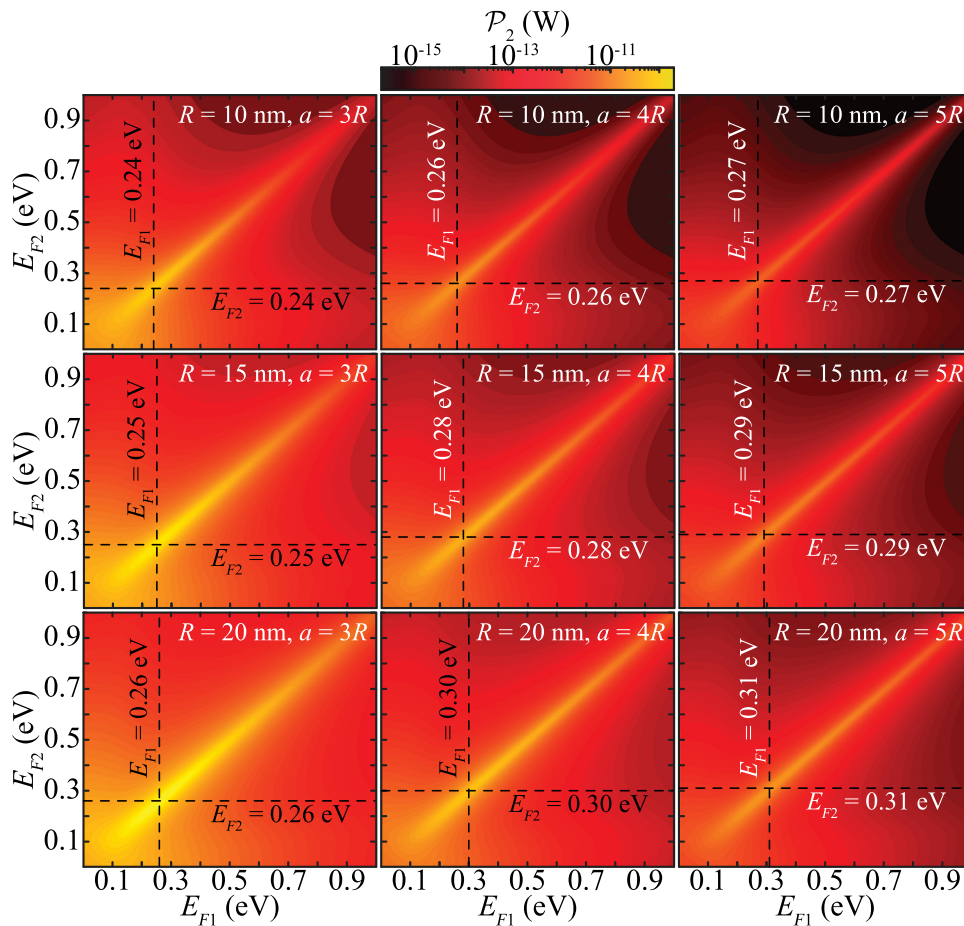


FIG. 6. Power absorbed by disk 2 at time $t = 0$ s in a pair of nanodisks of equal radius R separated from center to center by a distance a . Disk 1 has Fermi level E_{F1} and is at temperature $T_1 = 400$ K, while disk 2 has Fermi level E_{F2} and is at $T_2 = 300$ K. The environment is vacuum at temperature 300 K. The middle panel corresponds to the same values of R and a as in Fig. 1(b). In all panels, the Fermi level $E_{F1} = E_{F2}$ for which the power is maximized is marked using dashed lines.

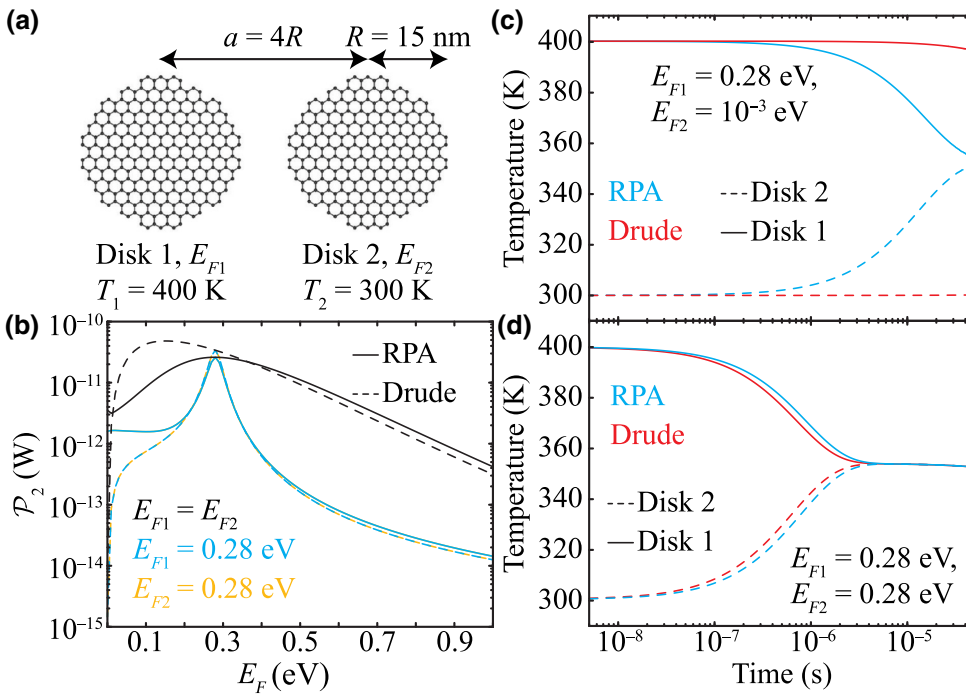
APPENDIX D: EFFECT OF THE CONDUCTIVITY MODEL

As discussed in the main text, to correctly obtain the dynamics of the radiative heat transfer between graphene nanodisks, it is crucial to use the appropriate model for the conductivity. In order to analyze this issue, in Fig. 7 we study the heat transferred between two nanodisks of radius $R = 15$ nm and $a = 4R$, as shown in panel (a). Disk 1 has Fermi level E_{F1} and initial temperature $T_1 = 400$ K, while disk 2 has E_{F2} and initial temperature $T_2 = 300$ K. As in the main text, the environment is vacuum at 300 K. In Fig. 7(b), we show \mathcal{P}_2 , the power absorbed by disk 2, calculated using two models of the graphene conductivity, for different combinations of E_{F1} and E_{F2} . Specifically, the solid curves display the results for a conductivity obtained from the local limit of the RPA for an extended graphene sheet [37] (as the one used in all of the results of this work), while the dashed curves represent the same calculations performed with a simple Drude model [37] instead. In both cases, for the black curves we assume $E_{F1} = E_{F2}$, whereas for the blue and yellow ones, we fix, respectively, E_{F1} or E_{F2} to 0.28 eV, while varying the other one. Examining these results, we observe that, when using the Drude model, \mathcal{P}_2 vanishes if

the Fermi level of either disk approaches zero. This is in sharp contrast to the results obtained with the RPA model, for which \mathcal{P}_2 does not vanish in that limit. The reason for these differences is the contribution of the interband transitions, which occur at energies more than twice the value of the Fermi level and are not captured by the Drude-model conductivity.

This drastic difference in \mathcal{P}_2 for small Fermi levels can result in important changes of the thermalization dynamics. For instance, in Fig. 7(c) we plot the temporal evolution of the temperatures of the two disks when $E_{F1} = 0.28$ eV and $E_{F2} = 10^{-3}$ eV, calculated using both models. The red and blue curves represent, respectively, the results obtained using the Drude and the RPA conductivity. Clearly, while the results obtained with the RPA conductivity predict a thermalization in around 50 μ s, due to the fact that \mathcal{P}_2 does not vanish, the Drude model predicts a negligible change of temperature in the same time interval.

When the Fermi levels of the nanodisks do not approach zero, the thermalization dynamics predicted by the two models are in much better agreement, as expected from the results of panel (a). This is shown in Fig. 7(d), where we plot the temporal evolution of the temperatures of the two disks when $E_{F1} = E_{F2} = 0.28$ eV.



APPENDIX E: EFFECT OF THE FERMI LEVEL

As discussed in Fig. 1, for a given range of temperatures, there exists a finite value of the Fermi level for which two disks exhibit the optimum heat transfer and therefore are

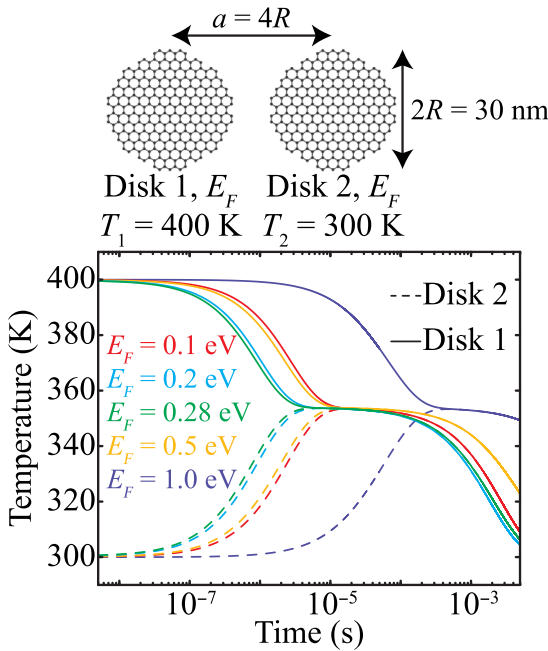


FIG. 8. Thermalization of two graphene nanodisks of radius $R = 15$ nm, center-to-center separation $a = 4R$, and equal Fermi levels E_F , as shown in the upper schematics, placed in vacuum at 300 K. The colored curves represent the dynamics for different values of E_F , as depicted in the legend.

FIG. 7. (a) Schematics of the system under consideration, consisting of two disks of equal radius $R = 15$ nm separated by $a = 4R$. Disk 1 begins at temperature $T_1 = 400$ K and has Fermi level E_{F1} , while disk 2 begins at $T_2 = 300$ K and has Fermi level E_{F2} . The environment is vacuum at temperature 300 K. (b) Power absorbed by disk 2 at time $t = 0$ s for different conductivity models and Fermi-level combinations. (c) Temporal evolution of the temperatures of the two disks for $E_{F1} = 0.28$ eV and $E_{F2} = 10^{-3}$ eV. (d) Same as (c), but for Fermi levels $E_{F1} = E_{F2} = 0.28$ eV.

expected to thermalize the most rapidly. For the system of two nanodisks considered in the main text, with $R = 15$ nm and $a = 4R$, at temperatures between 300 and 400 K, the optimum value, which occurs along the line $E_{F1} = E_{F2}$, is found to be 0.28 eV. In Fig. 8, we analyze the thermalization of these two disks for different values of their Fermi level. As expected, the fastest thermalization occurs for the optimum Fermi level. Larger or smaller values of the Fermi level result in a less efficient radiative heat transfer and therefore lead to a slower thermalization process. In particular, when $E_F = 1.0$ eV, the thermalization takes approximately 1000 times as long as the optimum case. Interestingly, over this time scale, the heat transfer to the environment becomes significant for those disks that have already thermalized with one another and therefore they cool down.

APPENDIX F: EFFECT OF THE ELECTRON MOBILITY

The electron mobility has a strong influence on the optical response of the graphene nanodisks and therefore can influence the time scale over which the radiative transfer occurs. In order to analyze the effect of the electron mobility, we consider, in Fig. 9, the thermalization of two nanodisks of equal radius $R = 15$ nm and $a = 4R$, as depicted in the upper schematics. Similar to the system of Appendix D, disks 1 and 2 begin at temperatures $T_1 = 400$ K and $T_2 = 300$ K, respectively, while their Fermi levels are both set to 0.28 eV. The blue curve in Fig. 9 displays the temporal evolution of the temperatures of the two disks for $\mu = 3000 \text{ cm}^2/(\text{V s})$, which is the value used

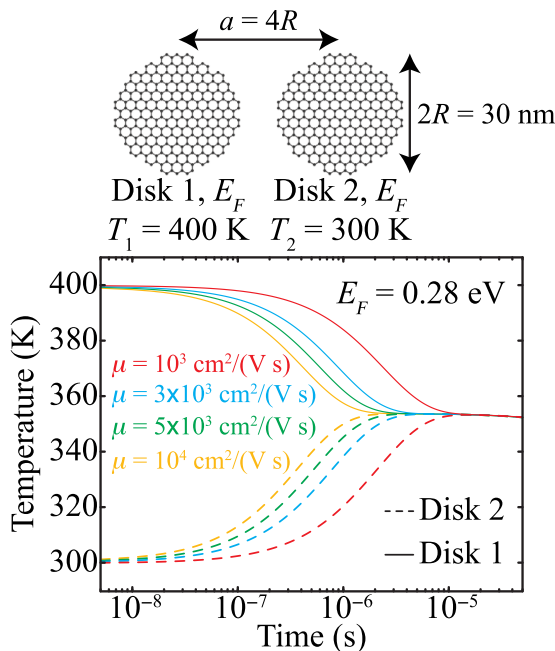


FIG. 9. Thermalization of two graphene nanodisks of radius $R = 15$ nm, center-to-center separation $a = 4R$, and Fermi level $E_F = 0.28$ eV, as shown in the upper schematics, for different values of the electron mobility μ , as indicated by the legend. The environment is vacuum at 300 K.

throughout this work, while the other colored curves show the corresponding results for larger and smaller values of μ , as indicated by the legend. As expected, an increase in the value of μ results in a faster thermalization process.

- [10] R. S. Ottens, V. Quetschke, S. Wise, A. A. Alemi, R. Lundock, G. Mueller, D. H. Reitze, D. B. Tanner, and B. F. Whiting, Near-Field Radiative Heat Transfer between Macroscopic Planar Surfaces, *Phys. Rev. Lett.* **107**, 014301 (2011).
- [11] R. St-Gelais, B. Guha, L. Zhu, S. Fan, and M. Lipson, Demonstration of strong near-field radiative heat transfer between integrated nanostructures, *Nano Lett.* **14**, 6971 (2014).
- [12] H. Chalabi, E. Hasman, and M. L. Brongersma, Near-field radiative thermal transfer between a nanostructured periodic material and a planar substrate, *Phys. Rev. B* **91**, 014302 (2015).
- [13] B. Song, D. Thompson, A. Fiorino, Y. Ganjeh, P. Reddy, and E. Meyhofer, Radiative heat conductances between dielectric and metallic parallel plates with nanoscale gaps, *Nat. Nanotechnol.* **11**, 509 (2016).
- [14] R. St-Gelais, L. Zhu, S. Fan, and M. Lipson, Near-field radiative heat transfer between parallel structures in the deep subwavelength regime, *Nat. Nanotechnol.* **11**, 515 (2016).
- [15] M. P. Bernardi, D. Milovich, and M. Francoeur, Radiative heat transfer exceeding the blackbody limit between macroscale planar surfaces separated by a nanosize vacuum gap, *Nat. Commun.* **7**, 12900 (2016).
- [16] M. Ghashami, H. Geng, T. Kim, N. Iacopino, S. K. Cho, and K. Park, Precision Measurement of Phonon-Polaritonic Near-Field Energy Transfer between Macroscale Planar Structures under Large Thermal Gradients, *Phys. Rev. Lett.* **120**, 175901 (2018).
- [17] A. Fiorino, D. Thompson, L. Zhu, B. Song, P. Reddy, and E. Meyhofer, Giant enhancement in radiative heat transfer in sub-30 nm gaps of plane parallel surfaces, *Nano Lett.* **18**, 3711 (2018).
- [18] A. Manjavacas, S. Thongrattanasiri, J. J. Greffet, and F. J. García de Abajo, Graphene optical-to-thermal converter, *Appl. Phys. Lett.* **105**, 211102 (2014).
- [19] G. Domingues, S. Volz, K. Joulain, and J. J. Greffet, Heat Transfer between Two Nanoparticles through Near Field Interaction, *Phys. Rev. Lett.* **94**, 085901 (2005).
- [20] P. O. Chapuis, M. Laroche, S. Volz, and J. J. Greffet, Radiative heat transfer between metallic nanoparticles, *Appl. Phys. Lett.* **93**, 201906 (2008).
- [21] P. Ben-Abdallah, K. Joulain, J. Drevillon, and C. Le Goff, Heat transport through plasmonic interactions in closely spaced metallic nanoparticle chains, *Phys. Rev. B* **77**, 075417 (2008).
- [22] A. Narayanaswamy and G. Chen, Thermal near-field radiative transfer between two spheres, *Phys. Rev. B* **77**, 075125 (2008).
- [23] A. Pérez-Madrid, J. M. Rubí, and L. C. Lapas, Heat transfer between nanoparticles: Thermal conductance for near-field interactions, *Phys. Rev. B* **77**, 155417 (2008).
- [24] A. Pérez-Madrid, L. C. Lapas, and J. M. Rubí, Heat Exchange between Two Interacting Nanoparticles beyond the Fluctuation-Dissipation Regime, *Phys. Rev. Lett.* **103**, 048301 (2009).
- [25] G. V. Dedkov and A. A. Kyasov, Radiative heat transfer of spherical particles mediated by fluctuation electromagnetic field, *J. Comput. Theor. Nanosci.* **7**, 2019 (2010).

- [26] A. Manjavacas and F. J. García de Abajo, Radiative heat transfer between neighboring particles, *Phys. Rev. B* **86**, 075466 (2012).
- [27] P. J. van Zwol, S. Thiele, C. Berger, W. A. de Heer, and J. Chevrier, Nanoscale Radiative Heat Flow Due to Surface Plasmons in Graphene and Doped Silicon, *Phys. Rev. Lett.* **109**, 264301 (2012).
- [28] K. Kim, B. Song, V. Fernández-Hurtado, W. Lee, W. Jeong, L. Cui, D. Thompson, J. Feist, M. T. H. Reid, F. J. García-Vidal, J. C. Cuevas, E. Meyhofer, and P. Reddy, Radiative heat transfer in the extreme near field, *Nature* **528**, 387 (2015).
- [29] H. Kallel, R. Carminati, and K. Joulain, Temperature of a nanoparticle above a substrate under radiative heating and cooling, *Phys. Rev. B* **95**, 115402 (2017).
- [30] J. Dong, J. Zhao, and L. Liu, Near-field radiative heat transfer between clusters of dielectric nanoparticles, *J. Quant. Spectrosc. Radiat. Transfer* **197**, 114 (2017).
- [31] J. Dong, J. Zhao, and L. Liu, Radiative heat transfer in many-body systems: Coupled electric and magnetic dipole approach, *Phys. Rev. B* **95**, 125411 (2017).
- [32] D. Becerril and C. Noguez, Near-field energy transfer between nanoparticles modulated by coupled multipolar modes, *Phys. Rev. B* **99**, 045418 (2019).
- [33] C. Henkel and P. P. Schmidt, On anomalously large nanoscale heat transfer between metals, *J. Opt. Soc. Am. B* **36**, C10 (2019).
- [34] F. H. L. Koppens, D. E. Chang, and F. J. García de Abajo, Graphene plasmonics: A platform for strong light-matter interactions, *Nano Lett.* **11**, 3370 (2011).
- [35] A. N. Grigorenko, M. Polini, and K. S. Novoselov, Graphene plasmonics, *Nat. Photonics* **6**, 749 (2012).
- [36] S. Thongrattanasiri, F. H. L. Koppens, and F. J. García de Abajo, Complete Optical Absorption in Periodically Patterned Graphene, *Phys. Rev. Lett.* **108**, 047401 (2012).
- [37] F. J. García de Abajo, Graphene plasmonics: Challenges and opportunities, *ACS Photonics* **1**, 135 (2014).
- [38] J. Chen, M. Badioli, P. Alonso-González, S. Thongrattanasiri, F. Huth, J. Osmond, M. Spasenović, A. Centeno, A. Pesquera, P. Godignon, A. Zurutuza Elorza, N. Camara, F. J. García de Abajo, R. Hillenbrand, and F. H. L. Koppens, Optical nano-imaging of gate-tunable graphene plasmons, *Nature* **487**, 77 (2012).
- [39] Z. Fei, A. S. Rodin, G. O. Andreev, W. Bao, A. S. McLeod, M. Wagner, L. M. Zhang, Z. Zhao, M. Thiemens, G. Dominguez, M. M. Fogler, A. H. C. Neto, C. N. Lau, F. Keilmann, and D. N. Basov, Gate-tuning of graphene plasmons revealed by infrared nano-imaging, *Nature* **487**, 82 (2012).
- [40] A. I. Volokitin and B. N. J. Persson, Near-field radiative heat transfer between closely spaced graphene and amorphous SiO₂, *Phys. Rev. B* **83**, 241407 (2011).
- [41] R. Yu, A. Manjavacas, and F. J. García de Abajo, Ultrafast radiative heat transfer, *Nat. Commun.* **8**, 2 (2017).
- [42] K. Shi, Y. Sun, Z. Chen, N. He, F. Bao, J. Evans, and S. He, Colossal enhancement of near-field thermal radiation across hundreds of nanometers between millimeter-scale plates through surface plasmon and phonon polaritons coupling, *Nano Lett.* **19**, 8082 (2019).
- [43] H. Yan, X. Li, B. Chandra, G. Tulevski, Y. Wu, M. Freitag, W. Zhu, P. Avouris, and F. Xia, Tunable infrared plasmonic devices using graphene/insulator stacks, *Nat. Nanotechnol.* **7**, 330 (2012).
- [44] V. W. Brar, M. S. Jang, M. Sherrott, J. J. Lopez, and H. A. Atwater, Highly confined tunable mid-infrared plasmonics in graphene nanoresonators, *Nano Lett.* **13**, 2541 (2013).
- [45] W. Li, B. Chen, C. Meng, W. Fang, Y. Xiao, X. Li, Z. Hu, Y. Xu, L. Tong, H. Wang, W. Liu, J. Bao, and Y. R. Shen, Ultrafast all-optical graphene modulator, *Nano Lett.* **14**, 955 (2014).
- [46] A. C. Tasolamprou, A. D. Koulouklidis, C. Daskalaki, C. P. Mavidis, G. Kenanakis, G. Deligeorgis, Z. Viskadourakis, P. Kuzhir, S. Tzortzakis, M. Kafesaki, E. N. Economou, and C. M. Soukoulis, Experimental demonstration of ultrafast THz modulation in a graphene-based thin film absorber through negative photoinduced conductivity, *ACS Photonics* **6**, 720 (2019).
- [47] O. Illic, M. Jablan, J. D. Joannopoulos, I. Celanovic, H. Buljan, and M. Soljačić, Near-field thermal radiation transfer controlled by plasmons in graphene, *Phys. Rev. B* **85**, 155422 (2012).
- [48] P. Ben-Abdallah, A. Belarouci, L. Frechette, and S.-A. Biehs, Heat flux splitter for near-field thermal radiation, *Appl. Phys. Lett.* **107**, 053109 (2015).
- [49] R. Messina, P. Ben-Abdallah, B. Guizal, and M. Antezza, Graphene-based amplification and tuning of near-field radiative heat transfer between dissimilar polar materials, *Phys. Rev. B* **96**, 045402 (2017).
- [50] F. V. Ramirez and A. J. H. McGaughey, Plasmonic thermal transport in graphene nanodisk waveguides, *Phys. Rev. B* **96**, 165428 (2017).
- [51] F. V. Ramirez, S. Shen, and A. J. H. McGaughey, Near-field radiative heat transfer in graphene plasmonic nanodisk dimers, *Phys. Rev. B* **96**, 165427 (2017).
- [52] Y. Yang and L. Wang, Electrically-controlled near-field radiative thermal modulator made of graphene-coated silicon carbide plates, *J. Quant. Spectrosc. Radiat. Transfer* **197**, 68 (2017).
- [53] V. Fernández-Hurtado, A. I. Fernández-Domínguez, J. Feist, F. J. García-Vidal, and J. C. Cuevas, Exploring the limits of super-Planckian far-field radiative heat transfer using 2D materials, *ACS Photonics* **5**, 3082 (2018).
- [54] O. Illic, N. H. Thomas, T. Christensen, M. C. Sherrott, M. Soljačić, A. J. Minnich, O. D. Miller, and H. A. Atwater, Active radiative thermal switching with graphene plasmon resonators, *ACS Nano* **12**, 2474 (2018).
- [55] O. Salihoglu, H. B. Uzlu, O. Yakar, S. Aas, O. Balci, N. Kakenov, S. Balci, S. Olcum, S. Süzer, and C. Kocabas, Graphene-based adaptive thermal camouflage, *Nano Lett.* **18**, 4541 (2018).
- [56] J. Song, Q. Cheng, Z. Luo, X. Zhou, and Z. Zhang, Modulation and splitting of three-body radiative heat flux via graphene/SiC core-shell nanoparticles, *Int. J. Heat Mass Transf.* **140**, 80 (2019).
- [57] M.-J. He, H. Qi, Y.-F. Wang, Y.-T. Ren, W.-H. Cai, and L.-M. Ruan, Near-field radiative heat transfer in multilayered graphene system considering equilibrium temperature distribution, *Opt. Express* **27**, A953 (2019).

- [58] J. Song, L. Lu, B. Li, B. Zhang, R. Hu, X. Zhou, and Q. Cheng, Thermal routing via near-field radiative heat transfer, *Int. J. Heat Mass Transf.* **150**, 119346 (2020).
- [59] Y. Yang, S. Basu, and L. Wang, Radiation-based near-field thermal rectification with phase transition materials, *Appl. Phys. Lett.* **103**, 163101 (2013).
- [60] P. Ben-Abdallah and S.-A. Biehs, Phase-change radiative thermal diode, *Appl. Phys. Lett.* **103**, 191907 (2013).
- [61] R. M. Abraham Ekereth, A. García-Martín, and J. C. Cuevas, Thermal discrete dipole approximation for the description of thermal emission and radiative heat transfer of magneto-optical systems, *Phys. Rev. B* **95**, 235428 (2017).
- [62] R. M. Abraham Ekereth, P. Ben-Abdallah, J. C. Cuevas, and A. García-Martín, Anisotropic thermal magnetoresistance for an active control of radiative heat transfer, *ACS Photonics* **5**, 705 (2018).
- [63] C. Khandekar, R. Messina, and A. W. Rodriguez, Near-field refrigeration and tunable heat exchange through four-wave mixing, *AIP Adv.* **8**, 055029 (2018).
- [64] P. Ben-Abdallah, S. A. Biehs, and K. Joulain, Many-Body Radiative Heat Transfer Theory, *Phys. Rev. Lett.* **107**, 114301 (2011).
- [65] R. Messina, M. Tschikin, S.-A. Biehs, and P. Ben-Abdallah, Fluctuation-electrodynamic theory and dynamics of heat transfer in systems of multiple dipoles, *Phys. Rev. B* **88**, 104307 (2013).
- [66] M. Nikbakht, Radiative heat transfer in anisotropic many-body systems: Tuning and enhancement, *J. Appl. Phys.* **116**, 094307 (2014).
- [67] M. Nikbakht, Three-body radiation dynamics in systems with anisotropic nanoparticles, *EPL (Europhys. Lett.)* **110**, 14004 (2015).
- [68] A. I. Volokitin and B. N. J. Persson, Near-field radiative heat transfer and noncontact friction, *Rev. Mod. Phys.* **79**, 1291 (2007).
- [69] R. Yu, J. D. Cox, J. R. M. Saavedra, and F. J. García de Abajo, Analytical modeling of graphene plasmons, *ACS Photonics* **4**, 3106 (2017).
- [70] I. Silveiro, J. M. Plaza Ortega, and F. J. García de Abajo, Plasmon wave function of graphene nanoribbons, *New J. Phys.* **17**, 083013 (2015).
- [71] L. Zundel and A. Manjavacas, Spatially resolved optical sensing using graphene nanodisk arrays, *ACS Photonics* **4**, 1831 (2017).
- [72] S. Sanders, A. May, A. Alessandro, and A. Manjavacas, Extraordinary enhancement of quadrupolar transitions using nanostructured graphene, *ACS Photonics* **5**, 4022 (2018).
- [73] K. I. Bolotin, K. J. Sikes, Z. Jiang, M. Klima, G. Fudenberg, J. Hone, P. Kim, and H. L. Stormer, Ultrahigh electron mobility in suspended graphene, *Sol. State Commun.* **146**, 351 (2008).
- [74] L. Banszerus, M. Schmitz, S. Engels, J. Dauber, M. Oellers, F. Haupt, K. Watanabe, T. Taniguchi, B. Beschoten, and C. Stampfer, Ultrahigh-mobility graphene devices from chemical vapor deposition on reusable copper, *Sci. Adv.* **1**, e1500222 (2015).
- [75] E. Pop, V. Varshney, and A. K. Roy, Thermal properties of graphene: Fundamentals and applications, *MRS Bull.* **37**, 1273 (2012).
- [76] O. Illic, M. Jablan, J. D. Joannopoulos, I. Celanovic, and M. Soljačić, Overcoming the black body limit in plasmonic and graphene near-field thermophotovoltaic systems, *Opt. Express* **20**, A366 (2012).
- [77] A. Fiorino, L. Zhu, D. Thompson, R. Mittapally, P. Reddy, and E. Meyhofer, Nanogap near-field thermophotovoltaics, *Nat. Nanotechnol.* **13**, 806 (2018).
- [78] S. M. Rylov, *Theory of Electric Fluctuations and Thermal Radiation* (Air Force Cambridge Research Center, Bedford, MA, 1959).
- [79] A. Manjavacas and F. J. García de Abajo, Vacuum Friction in Rotating Particles, *Phys. Rev. Lett.* **105**, 113601 (2010).